



High and low-cycle-fatigue properties of 17–4 PH manufactured via selective laser melting in as-built, machined and hipped conditions

Franco Concli¹ · Lorenzo Fraccaroli¹ · Filippo Nalli¹ · Luca Cortese²

Received: 18 February 2021 / Accepted: 22 August 2021 / Published online: 19 September 2021
© The Author(s) 2021

Abstract

In the last years, additive manufacturing (AM) has turned into an emerging technology and an increasing number of classes of material powders are now available for this manufacturing process. For large-scale adoption, an accurate knowledge of the mechanical behaviour of the resulting materials is fundamental, also considering that reliable data are often lacking and dedicated standards are still missing for these AM alloys. In this regard, the aim of the present work is to characterize both the high-cycle-fatigue (HCF) and the low-cycle-fatigue (LCF) behaviour of AM 17–4 PH stainless steel (SS). To better understand the performance of the selected alloy, four series of cylindrical samples were manufactured. Three series were produced via selective laser melting (SLM), better known as laser-based powder bed fusion of metals technology using an EOS M280 machine. The first series was tested in the as-built condition, the second was machined before testing to obtain a better surface finishing, while the third series was post-processed via hot isostatic pressing (HIP). Finally, a fourth series of samples was produced from the wrought 17–4 PH material counterpart, for comparison. The understanding and assessment of the influence of surface finishing on the fatigue behaviour of AM materials are fundamental, considering that in most applications the AM parts may present reticular or lattice structures, internal cavities or complex geometries, which must be set into operation in the as-built conditions, since a surface finishing postprocess is not convenient or not feasible at all. On the other side, a HIP process is often suggested to reduce the internal porosities and, therefore, to improve the resulting mechanical properties. The high-cycle-fatigue limits were obtained with a short staircase approach according to the Dixon statistical method. The maximum number of cycles (run-out) was set equal to 50,00,000. The part of the Wöhler diagram relative to finite life was also characterized by means of additional tests at higher stress levels. On the other side, the low-cycle tests allowed to tune the Ramberg–Osgood cyclic curves and the Basquin–Coffin–Manson LCF curves. The results obtained for the four different series of specimens permitted to quantify the reduction of the mechanical performance due to the actual limits of the laser-based powder bed fusion technology (surface quality, internal porosity, different solidification) with respect to traditional manufacturing and could be used to improve design safety and reliability, granting structural integrity of actual applications under elastic and elasto-plastic fatigue loads.

Keywords HCF · LCF · Additive manufacturing · 17–4 PH · Hipping

1 Introduction

Laser-sintered 17–4 PH stainless steel (SS) is a material showing a very good corrosion resistance and high strength guaranteed by its martensitic structure [1]. The high strength

is due to the precipitation of fine cuprum-rich face-centred cubic phase. A dendritic structure with body-centred cubic martensite and about 50% of reserved austenite is favoured by the laser-based powder bed fusion process. According to [2], the mechanical properties of additive manufactured materials are comparable with those produced with traditional technologies such as casting and machining. Nevertheless, the ultimate tensile (UTS) and yield (σ_y) strengths of laser-based powder bed fusion-produced 17–4 PH SS are quite lower than those of wrought material in H900 condition (age-hardening treatment: air quenching at 900 °C for 4 h) since the additive manufactured 17–4 PH SS is not

✉ Franco Concli
franco.concli@unibz.it

¹ Faculty of Science and Technology, Free University of Bozen-Bolzano, Piazza Università 5, 39100 Bolzano, Italy

² Department of Mechanical and Aerospace Engineering, Sapienza University of Rome, Rome, Italy

completely martensitic, thus showing retained austenite. The high speeds of solidification during the laser-based powder bed fusion process, indeed, prevents the formation of the martensite phase in the as-built material leading to a metastable austenitic microstructure.

Another feature to be pointed out is that the characteristic porosity which comes from the production process can impact the mechanical properties of the material [3]. The voids can serve as crack nucleation sites. Some authors [4, 5] suggested applying hot isostatic pressing (HIP) to reduce the presence of porosities. For this reason, this material is generally hardened. Nevertheless, in the literature, several works can be found in which this type of material shows a low high-cycle-fatigue resistance. Internal and surface defects such as porosities, inclusions and a high roughness in the as-built condition can act as crack nucleation sites [3, 6, 7]. Moreover, contradictory results regarding the effectiveness of the HIP process on AM 17–4 PH SS are present in literature [8, 9]. For this reason, having specific and reliable high-fatigue data are fundamental to identify the limits of AM materials.

Nevertheless, another peculiar advantage of additive manufacturing (AM) is its capability to produce lattice/reticular structures characterized by small sections and complex geometries. It is well known that those structures are often subjected to high plastic deformations [10]–[12]. The knowledge of the low-cycle-fatigue (LCF) performances is therefore a key aspect in the design of new structures and systems. Considering that the complex shape of reticula impedes surface finishing, it is also fundamental to understand the reduction of the fatigue properties related to the characteristic surface properties obtained with the laser-based powder bed fusion process.

With these premises, this work aims at the characterization of the mechanical properties (HCF and LCF) of a 17–4 PH SS produced via AM. In addition to a first series of as-built samples in which the surface roughness is the one that can be obtained from the laser-based powder bed fusion process, a second series of samples was produced with the same technology but successively machined. This is to assess the material fatigue life, accounting for the effect of the surface roughness typical of the AM technology that, as already pointed out, cannot be modified with finishing

operations (e.g. in lattice/reticular structures) in many actual applications.

Moreover, a third series of AM parts was heat treated via hot isostatic pressing (HIP) provided that several authors claim this treatment to be beneficial in terms of fatigue performances thanks to the reduction of the internal porosities induced by the AM production process.

Finally, a last series of samples having the same geometry was produced from wrought (NO AM) 17–4 PH SS material to better quantify the performance differences of AM powders with respect to traditional production alloys.

2 Chemical composition and microstructure

Standard EOS M280 parameter settings were used to produce all the AM samples employed in the experimental HCF and LCF campaigns. Specimens were printed in the building (vertical) direction. The machined AM samples were obtained starting from as-built geometries with stock added to permit machining to final dimensions. A manually controlled lathe was used, equipped with carbide turning inserts suitable for 17–4PH stainless steel grade type.

The chemical composition of 17–4 PH SS is shown in Table 1. The particles of the powder have a mean size of 44.454 μm . Chromium (Cr) interacts with carbon (C), forming chromium carbides along grains [13].

To prevent the creation of Cr_{23}C_6 [14] and to increase strength, niobium (Nb) is used. It promotes the formation of NbC. Silicon (Si) decreases the mechanical properties promoting the formation of ferrite, but it is useful for fluidizing the material during the casting. To compensate this effect, chromium and nickel (Ni) are used. They reduce the formation of ferrite in favour of austenite. Nickel and manganese (Mn) are helpful to avoid the formation of Cr_{23}C_6 and FeS phases, respectively, forming Cr_2N and MnS instead. Cuprum helps increasing the overall strength of the material, forming precipitates.

In addition, chemical analysis and scanning electron microscopy (SEM) measurements, performed at Politecnico di Milano, were made to highlight the possible presence of defects close to the surfaces, which could affect the fatigue behaviour. Defects were found to be up to hundreds

Table 1 Chemical composition of the 17–4 PH SS

C	Si	Mn	P	S	Cr	Ni	Mo
0.036	0.78	0.33	0.009	0.004	16.2	4.02	0.002
Co	V	Ti	Cu	W	Sn	Al	Nb
0.012	0.018	0.002	0.372	0.009	0.004	0.001	0.29

of micrometers. This evidence was confirmed by microcomputer tomography (μ -CT) measurements.

A first scouting measure was made with a voxel size of $2.25\ \mu\text{m}$ and a second detailed measure with a voxel size of $1\ \mu\text{m}$. Measures were made at the University of Kassel.

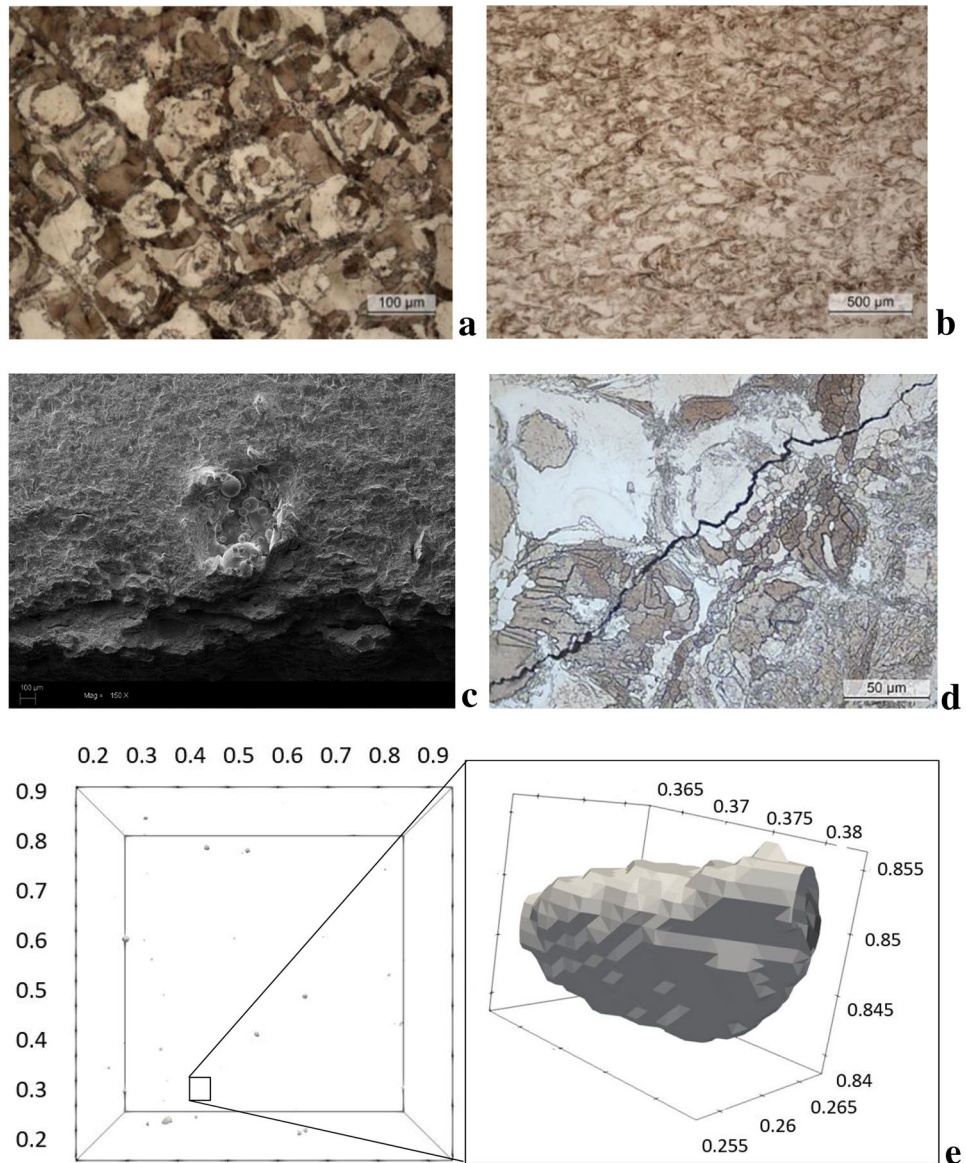
From Fig. 1 it can be appreciated that the propagation direction is not influenced by the melt pool boundaries, but it is instead completely inside the pools. The chemical composition of the melt pools was investigated by energy-dispersive X-ray spectroscopy (EDS) analysis. No appreciable difference was detected among the pool centre and boundaries: Al (0.28–0.30%), Si (0.47–0.51%), Cr (17.1–17.4%), Fe (73, 15–74.6%), Ni (3.76–3.79%), Cu (3.27–3.30%) and Nb (0.24–0.25%).

Finally, micro-hardness tests were performed on the four series of samples. Measurements were made for ten

radial positions starting from the surface to the axis. No relevant differences were observed among the NO–AM, as-built and hipped series with a slightly higher hardness for the hipped samples, while the machined ones exhibited higher values. This phenomenon could be ascribed to the machining process that might have removed or reduced the initial surface or subsurface porosities, and modified the surface material state due to the heat generated. Also, the residual stress state resulting from the cutting operations could have had an influence on the increased hardness (Fig. 2).

Additional data regarding the 17–4 PH alloy, data regarding the tooth root bending strength and the ductile behaviour and fracture are available [15, 16], which were published in the framework of the same research project.

Fig. 1 SEM: melt pools in the transversal (a) and in the build (b) directions, defect (c) and crack path (d) and μ -CT (mm) (e) analyses



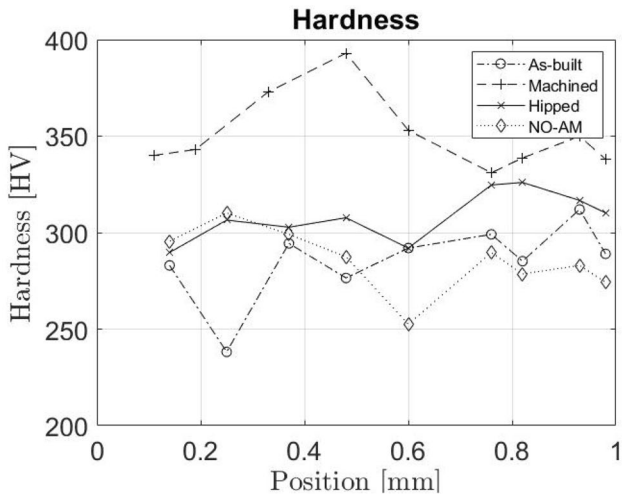


Fig. 2 Vickers micro-hardness measurements along the radial direction

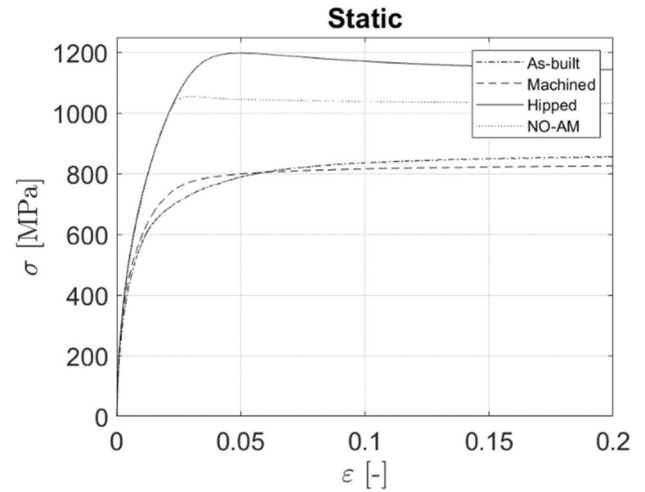


Fig. 4 17-4PH stress–strain curves of as built, machined, hipped and no-am samples, from tensile tests

3 Experimental tests

3.1 HCF

High-cycle-fatigue (HCF) tests were performed on cylindrical samples (Fig. 3, on the right) with a geometry designed according to the ASTM E466 standard [17]. The experimental facility used for testing is a STEPLab-UD04 fatigue testing machine capable of applying up to 5 kN at maximum frequency of 35 Hz [18].

In addition to the HCF tests, a quasi-static tensile characterization was performed. The geometry of the adopted samples is shown in Fig. 3 (on the left). Tensile tests were

performed at room temperature with a crosshead speed set to 0.1 mm/min.

The tested samples present the cone-cup-shaped fracture surface, typical of the ductile failure. Plastic deformation was also confirmed by the presence of a fibrous and irregular surface (necking region).

Preliminary static tests were also performed to determine the yielding point (Fig. 4). These data (Table 2) have been used for the calibration of the Basquin parameters, as described in the following.

HFC tests were performed according to the ASTM E466 [17]. The fatigue limit σ_F was calculated with the short staircase approach [19–22]. More in detail, several tests at different load levels were performed. The staircase method

Fig. 3 Standard specimen for quasi-static (left) and HCF (right) tests according to ASTM E466

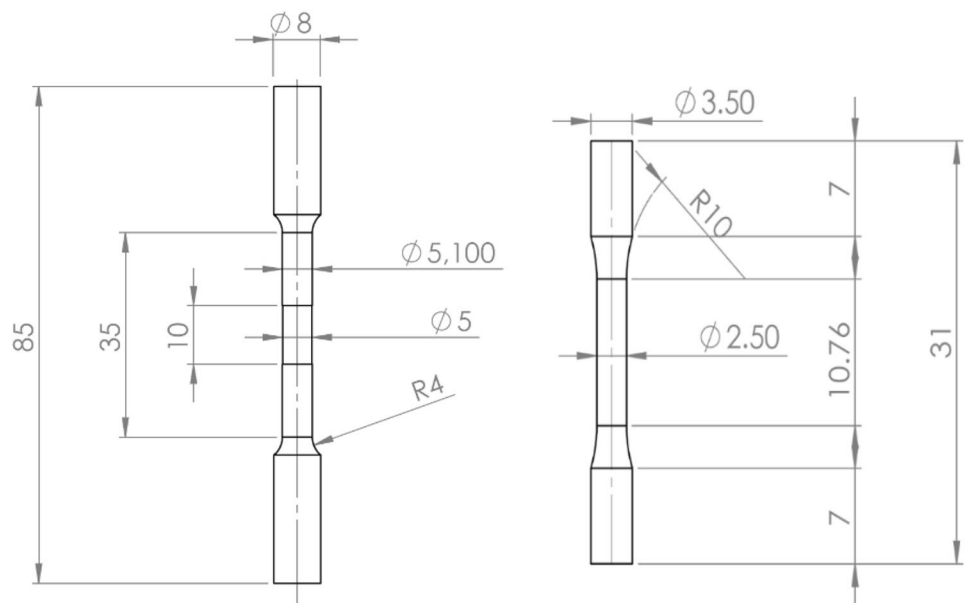


Table 2 Yielding stress of as built, machined, hiped and no-am samples, from tensile tests

Sample	σ_y [MPa]
As-built	390
Machined	426
Hipped	468
NO AM (wrought)	489

prescribes to define a force increment ΔF (that is directly related to the accuracy of the results that can be achieved). The actual ΔF was set to 50 N, corresponding to a stress interval $\Delta\sigma$ equal to 10 MPa.

If the initial test, performed at a force level F_i , reaches the run-out condition (50,00,000 cycles without failure), the next test has to be performed on a force level increased by ΔF i.e. $F_{i+1} = F_i + \Delta F$.

Otherwise, if the specimen broke, the next force level must be decreased by ΔF , i.e. $F_{i+1} = F_i - \Delta F$.

Figure 4 shows the short staircase sequences (6 tests—maximum value according to Dixon [23]) for the four series of samples: as-built, machined, hiped and NO AM (wrought). The Dixon statistical approach considers, in

addition to the number of run-outs (O) and failures (X) as the traditional staircase method, also the sequence order. The statistical significance of the results is ensured by a statistical correction coefficient k . The fatigue limit can be calculated by means of the following relation:

$$\sigma_F = x_f + k \cdot \Delta\sigma \tag{1}$$

in which σ_F is the fatigue limit at a 50% probability, x_f is the stress level of the last test (ID = 6 with reference to Fig. 5) and k a coefficient depending on the sequence order (Table 3).

For the as-built testing campaign, the tests order results in O–X–O–X–X–X ($x_f = 265$ MPa). Having a k factor equal to 0.661, the fatigue limit results $\sigma_F = 271$ MPa.

For the machined samples, the test order was O–X–O–O–X–O ($x_f = 336$ MPa). The Dixon coefficient k was 0.372, resulting in a fatigue limit equal to $\sigma_F = 340$ MPa.

For the hiped series, the test order was O–O–O–O–X–O ($x_f = 264$ MPa). The Dixon coefficient k was 0.894 resulting in a fatigue limit equal to $\sigma_F = 243$ MPa.

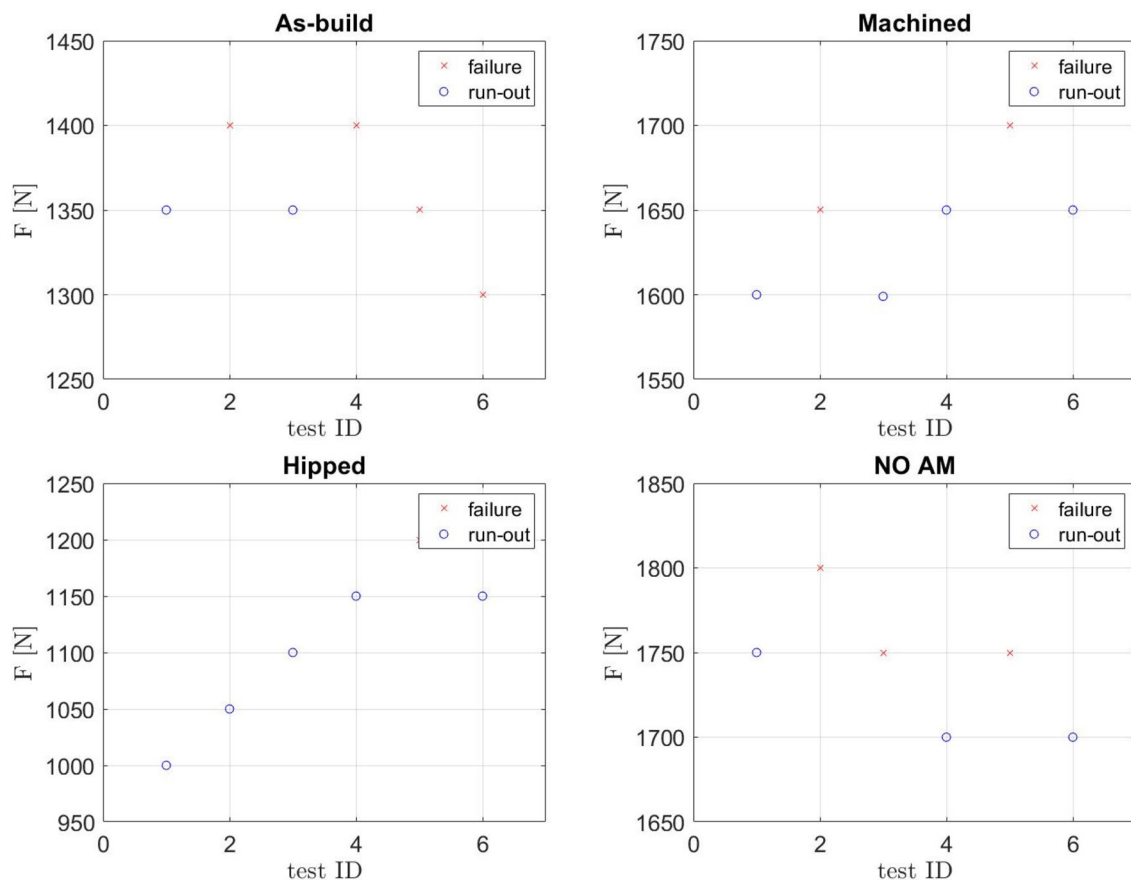


Fig. 5 Short stair-case sequences for the four series of tested samples

Table 3 Results of the HCF tests

Sample	σ_F [MPa]	x_f [MPa]	k [-]
As-built	271	265	0.661
Machined	340	366	0.372
Hipped	243	264	0.894
NO AM (wrought)	355	346	0.831

For the wrought (NO AM) series, the test order was O–X–X–O–X–O ($x_f = 346$ MPa). The Dixon coefficient k was 0.831 resulting in a fatigue limit equal to $\sigma_F = 355$ MPa.

Additional tests were performed for the four groups at higher levels of stress to obtain the left part of the Wöhler diagram, corresponding to finite life.

Figure 6 shows the S–N curves. The continuous line refers to the as-built condition, the dashed line to the machined one, the dots represent the hipped condition and the dot-dashed line the wrought material.

3.2 LCF

Low-cycle-fatigue tests were performed on cylindrical samples with standard dimensions according to ASTM E606 [26], as shown in Fig. 7 (on the left). As for the HCF, four series of samples were tested.

The comparison with data from literature [24], [6], [25] shows a good agreement of the results.

Strain-controlled fatigue tests were performed on the STEPLab UD04 testing machine (Fig. 7, on the right) according to [26]. Tests were performed at a strain ratio $R_\epsilon = -1$. The testing frequency was set to 0.1 Hz [27, 28]. This value, the lowest prescribed by the ASTM E606, was kept constant during the tests. Higher speeds may affect the results promoting a slight increment in the temperature of the sample and a modification of the mechanical properties.

The stabilized cycles for each tested deformation level were interpolated by means of the Ramberg–Osgood (RO) equation [18] (Eq. 2) to obtain the stabilized curves (Fig. 8).

$$\epsilon_a = \epsilon_{ae} + \epsilon_{ap} = \frac{\sigma_a}{E} + \left(\frac{\sigma_a}{K'}\right)^{\frac{1}{n'}} \quad (2)$$

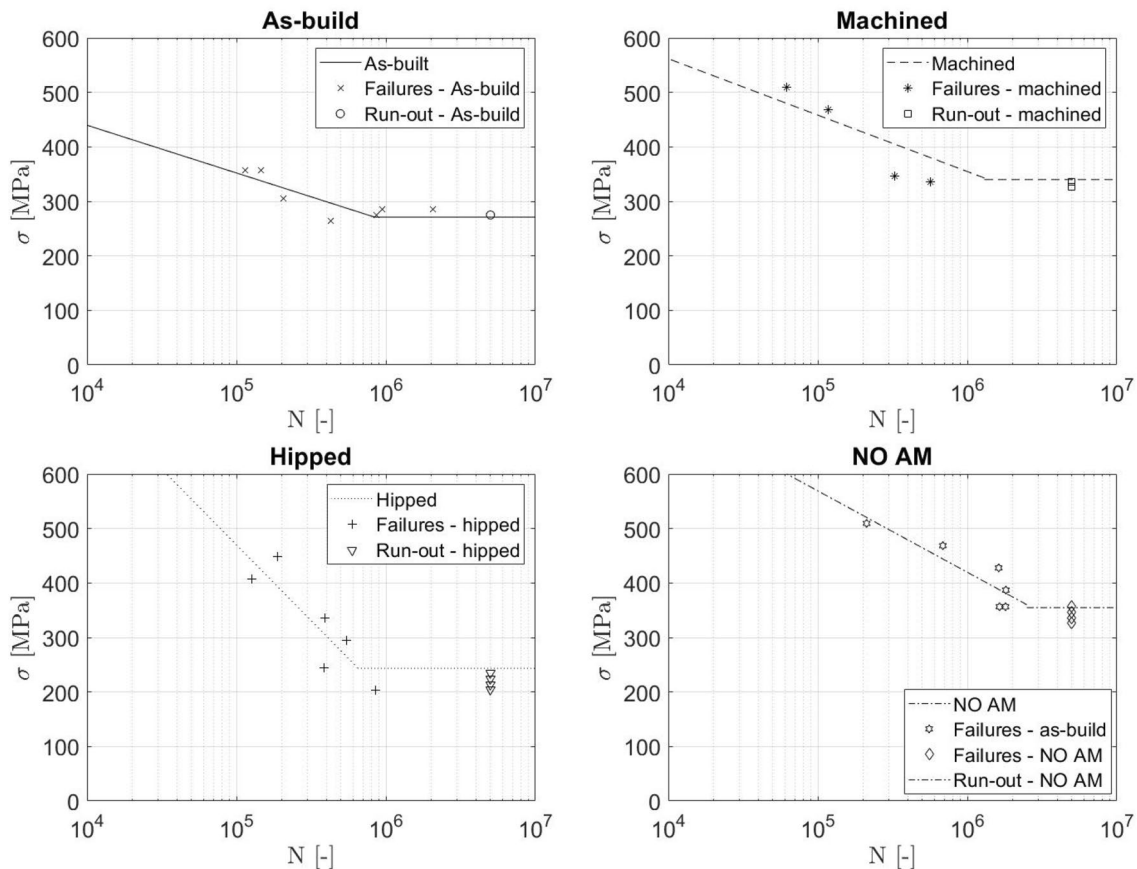
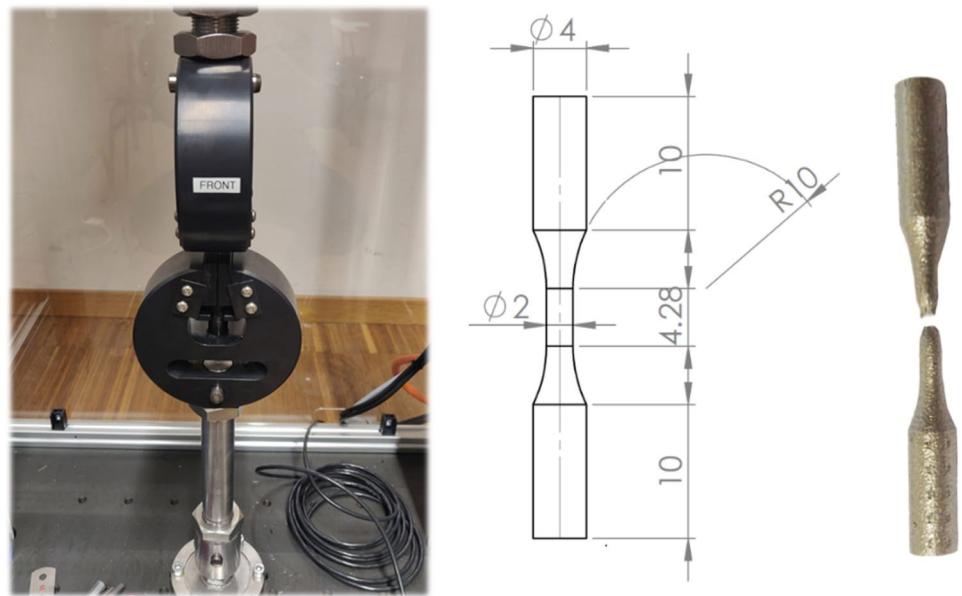


Fig. 6 HCF diagrams

Fig. 7 Testing machine (left), Standard specimen for the LCF tests according to ASTM (right)



Here, ϵ_a is the total strain amplitude, ϵ_{ae} and ϵ_{ap} are the elastic and the plastic portions of ϵ_a , σ_a is the stress amplitude, E is the elastic module, while K' and n' are constants that depend on the material being considered [29]. In this form, K and n are not the same as the constants commonly seen in the Hollomon equation [30].

The parameters of the RO equations are reported in Table 4.

The stabilized curves are shown in Fig. 8. The as-built series shows a slight hardening behaviour [31], which is more evident for the machined series. On the other side, the hipped series show, at least in the low-strain range ($\epsilon_a < 0.06$), a marked hardening. Finally, the NO AM series shows a mixed behaviour with softening just after the yielding and hardening for higher strains, with a transition at $\epsilon_a = 0.05$.

Even after the stabilization, tests were continued up to rupture of the sample to obtain data for the $\epsilon - N$ fatigue curves, better known as the Basquin–Coffin–Manson (BCM) diagrams (Eq. 3)

$$\epsilon_a = \frac{\Delta\epsilon}{2} = \frac{\sigma'_f}{E}(2N)^b + \epsilon'_f(2N)^c \tag{3}$$

where $\Delta\sigma'_f, b, \epsilon'_f, c$ are the four material constants to be identified.

Figure 9 shows the experimental data for the four series of samples and the fitting curves using the BCM equation.

The calculation procedure prescribes to firstly determine the Basquin coefficients (σ'_f and b) starting from the yield stress σ_Y and the high-cycle-fatigue limit σ_F with a linear interpolation.

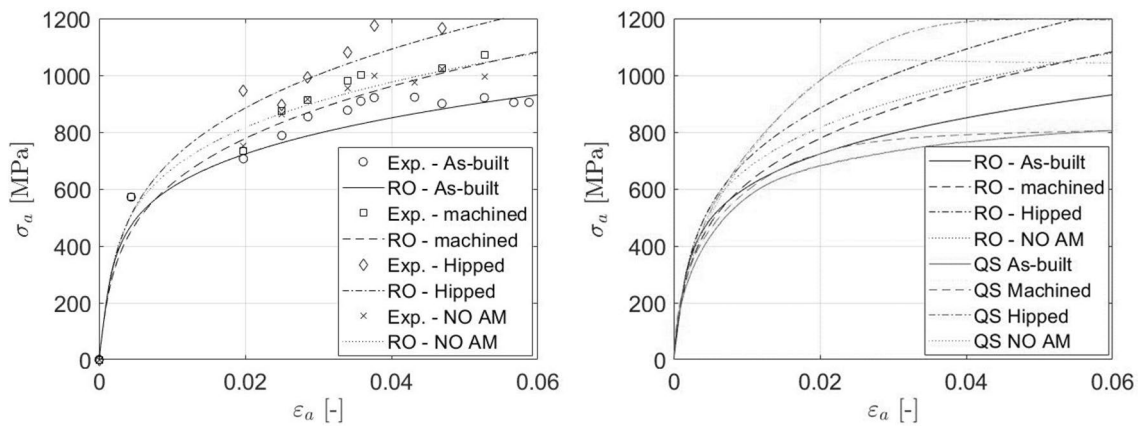


Fig. 8 Cyclic RO curves vs. constitutive QS ones

The Basquin equation (describing the relation between the elastic deformation ϵ_{ae} and the number of cycles N) can be used to separate the plastic deformation ϵ_{ap} from the total one.

$$\epsilon_{ap} = \epsilon_a - \epsilon_{ae} = \epsilon'_f(2N)^c \tag{4}$$

With the aim of determining the maximum likelihood estimators for ϵ'_f and c according to Eq. 4, the ASTM 739 standard [28] was used. The equation of a line fitting the experimental points can be rewritten as

$$\log(N) = \hat{A} + \hat{B} \log(\epsilon_{ap}) \tag{5}$$

Table 4 Parameters of the Ramberg–Osgood equation

Sample	K' [MPa]	n' [-]	E [MPa]
As-built	1705	0.2092	2,10,000
Machined	2392	0.2730	2,10,000
Hipped	2673	0.2665	2,10,000
NO AM (wrought)	2088	0.2276	2,10,000

The maximum likelihood estimators of A and B are the following:

$$\hat{A} = \bar{Y} - \hat{B}\bar{X} \tag{6}$$

$$\hat{B} = \frac{\sum (x_i - \bar{X})(y_i - \bar{Y})}{\sum (x_i - \bar{X})^2} \tag{7}$$

where \bar{X} and \bar{Y} are the averaged values of the dependent variable x_i ($\log(\epsilon_{ap})$) and independent variable y_i ($\log(N)$).

Equation 5 can be transformed as follows:

$$\epsilon_{ap} = 10^{-\frac{\hat{A}}{\hat{B}}} \left(\frac{1}{2}\right)^{\frac{1}{\hat{B}}} (2N)^{\frac{1}{\hat{B}}} \tag{8}$$

Therefore, the maximum likelihood estimators of the Coffin–Manson coefficients ϵ'_f and c (Eq. 4) can be calculated as

$$\epsilon'_f = 10^{-\frac{\hat{A}}{\hat{B}}} \left(\frac{1}{2}\right)^{\frac{1}{\hat{B}}} \tag{9}$$

and

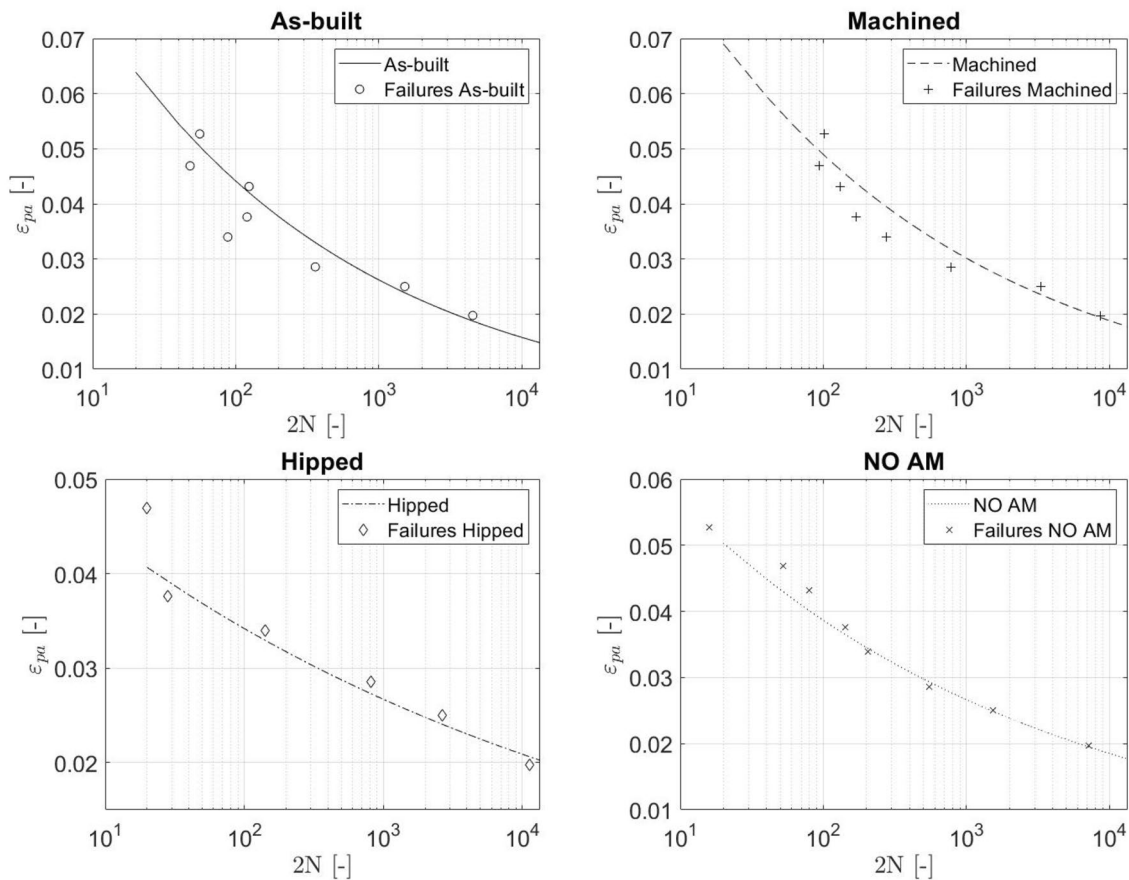


Fig. 9 LCF diagrams

$$c = 1/\hat{B} \tag{10}$$

The final values are reported in Table 4.

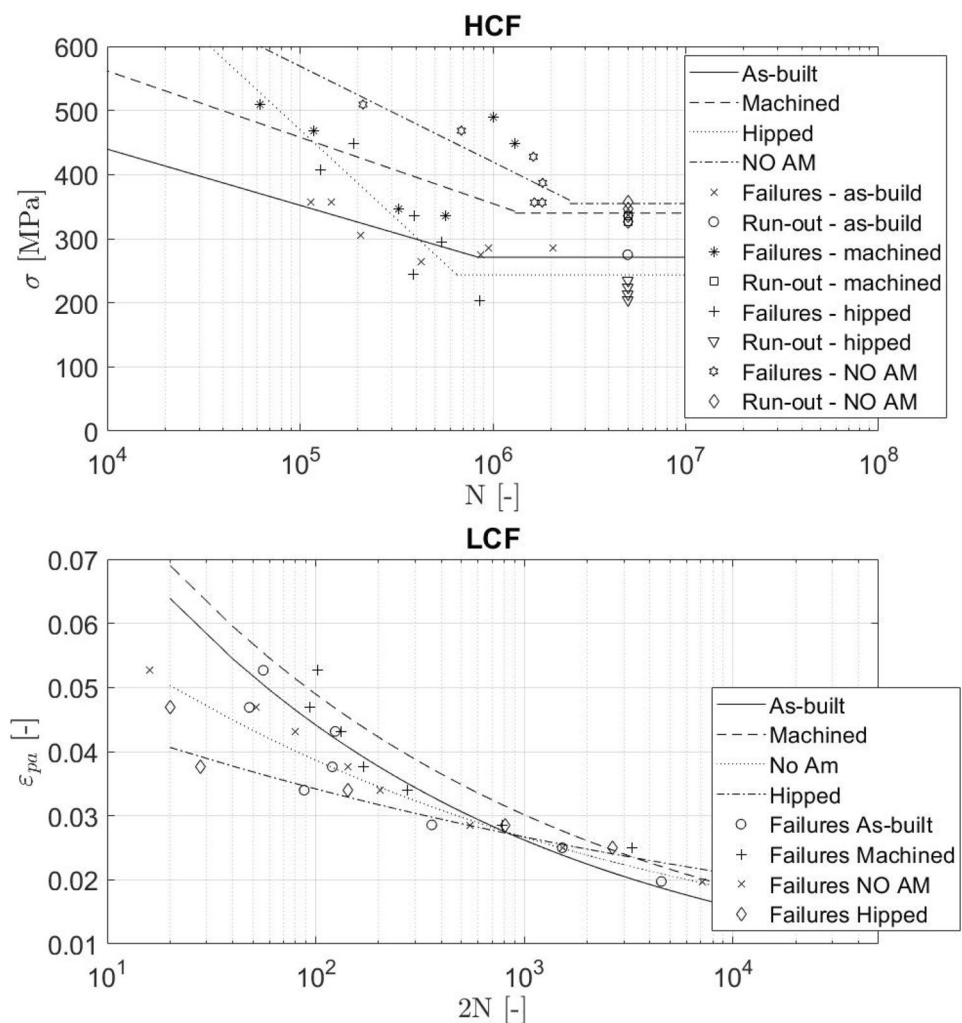
4 Discussion

Figure 10 compares the material properties of the four series. Concerning the HCF, as expected, the machining process significantly increases the fatigue performances with respect to the as-built condition, due to a superior surface finishing that reduces the local stress intensification thus improving fatigue life. The fatigue limit for the as-built samples is 25.4% lower with respect to the fatigue limit of the AM machined samples. In the same way, wrought material (NO AM) performs better in comparison with the AM machined samples. In this case, while the surface roughness is the same, the internal porosities affect the overall performance, with differences of about 4% (Table 5).

While the above-mentioned results were expected, less trivial is the effect of the hipping process. While several scholars claim that this treatment can improve the fatigue performances by reducing the internal porosities, the actual data show a reduction of the fatigue limit of about 12% in the presence of the HIP process, instead. This effect could be justified considering that, as demonstrated by du Plessis et al. [32], the near-surface pores are not always closed and hipped and sometimes become over-pressurized after the treatment itself. Especially for small samples subjected to axial loads, like in the present case, this effect could lead to a premature failure of the hipped material with respect to the as-built one.

On the other hand, the LCF tests show that while the wrought (NO AM) material performs better for HCF loads, the AM material seems to have a better performance in terms of LCF. The comparison between the AM machined and the wrought (NO AM) samples shows that the first can survive longer for the same applied cyclic deformation. This might

Fig. 10 Comparison between the four different series of samples



be explained by the different microstructure of the material which contains austenite.

The effect of the surface finishing is evident, and the as-built samples are less resistant with respect to the AM machined ones, even though the two BCM curves have a similar shape. The HIP process produces again the worst performance.

5 Conclusions and future work

In this experimental study, four series of samples made of 17–4PHSS were produced, tested and characterized in the high- and in the low-cycle-fatigue range. The series of samples differ in terms of surface finishing, heat treatment and manufacturing technology. A first series of AM as-built samples was used as reference. A second series, machined, was used to study the effect of the surface finishing. The third series was treated by means of HIP. The fourth series was manufactured from NO AM material for comparison.

The HCF limit was determined using the short staircase approach according to Dixon. For the LCF, first the RO equations were tuned. Successively, based on the results of strain-controlled tests, the BCM fatigue curves were calibrated.

The surface finishing (machined vs. as-built) seems to significantly improve the HFC properties (+25%). The comparison between the machined and the NO AM series which have the same surface finishing shows that the wrought material is better performing (+31.0%) in terms of fatigue limit.

The hiping process is typically adopted on AM materials to reduce the porosities and, therefore, to improve the mechanical behaviour. Indeed, this effect was confirmed by the static tests (the hiped samples show mechanical properties aligned with the machined and NO AM—wrought material), while unlike that expected, the process seems to not improve the fatigue limit but reduces it (−10.3%, hiped vs. as-built).

On the other side, in the LFC range, the four series perform differently. The machining promotes a constant increase of the maximum possible strain amplitude (about +0.085). In the low range of cycles, the as-built series performs better with respect to the hiped and the NO AM ones. After about

800 cycles, both series (hiped and NO AM) overtake the as-built curve.

While small samples were used because they better represent the typical dimensions of reticular structures, a future work will be to extend this study to bigger diameters to understand if the actual finding could be generalized.

Author contributions Conceptualization FC, LF, FN, LC. Testing: FC, LF. Data analysis: FC. Writing: FC, LF, FN, LC.

Funding Open access funding provided by Libera Università di Bolzano within the CRUI-CARE Agreement. The authors would like to thank the Free University of Bozen-Bolzano for the financial support given to this study through the projects M.AM.De (TN2092, call CRC2017 Unibz PI Franco Concli franco.concli@unibz.it).

Declarations

Conflict of interest On behalf of all authors, the corresponding author states that there is no conflict of interest.

Open Access This article is licensed under a Creative Commons Attribution 4.0 International License, which permits use, sharing, adaptation, distribution and reproduction in any medium or format, as long as you give appropriate credit to the original author(s) and the source, provide a link to the Creative Commons licence, and indicate if changes were made. The images or other third party material in this article are included in the article's Creative Commons licence, unless indicated otherwise in a credit line to the material. If material is not included in the article's Creative Commons licence and your intended use is not permitted by statutory regulation or exceeds the permitted use, you will need to obtain permission directly from the copyright holder. To view a copy of this licence, visit <http://creativecommons.org/licenses/by/4.0/>.

References

1. Cheruvathur S, Lass EA, Campbell CE (2016) Additive manufacturing of 17–4 PH stainless steel: post-processing heat treatment to achieve uniform reproducible microstructure. *JOM*. <https://doi.org/10.1007/s11837-015-1754-4>
2. Yadollahi A et al (2015) Fatigue behavior of selective laser melted 17-4 PH stainless steel. In: Proceedings of 26th international solid freeform fabrication symposium, Austin, TX. <https://doi.org/10.13140/RG.2.1.3996.2323>
3. Yadollahi A, Shamsaei N, Thompson SM, Elwany A, Bian L (2015) Mechanical and microstructural properties of selective laser melted 17–4 ph stainless steel. In: ASME International Mechanical Engineering Congress and Exposition, Proceedings (IMECE), vol 2A. <https://doi.org/10.1115/IMECE2015-52362>
4. Masuo H et al (2018) Influence of defects, surface roughness and HIP on the fatigue strength of Ti-6Al-4V manufactured by additive manufacturing. *Int J Fatigue* 117:163–179. <https://doi.org/10.1016/j.ijfatigue.2018.07.020>
5. Masuo H et al (2017) Effects of defects, surface roughness and HIP on fatigue strength of Ti-6Al-4V manufactured by additive manufacturing. *Procedia Structural Integrity* 7:19–26. <https://doi.org/10.1016/j.prostr.2017.11.055>
6. G. Sehart J.T., Witt, 2010 “Dynamic Strength and Fracture Toughness Analysis of Beam Melted Parts,”.

Table 5 Parameters of the Basquin-Coffin-Manson equation

Sample	b	c	$\dot{\sigma}_f$	$\dot{\epsilon}_f$
As-built	−0.0250	−0.2365	390	0.1263
Machined	−0.0160	−0.2204	426	0.1299
Hipped	−0.0450	−0.1111	468	0.0540
NO AM (wrought)	−0.0220	−0.1712	489	0.0804

7. C. Wu, J., Lin, 2002 “Tensile and Fatigue Properties of 17–4 PH Stainless Steel at High Temperatures,” *Met. Mater. Trans.*
8. R. Molaie, A. Fatemi, and N. Phan, “Multiaxial fatigue of LB-PBF additive manufactured 17–4 PH stainless steel including the effects of surface roughness and HIP treatment and comparisons with the wrought alloy,” *Int. J. Fatigue*, vol. 137, 2020, doi: <https://doi.org/10.1016/j.ijfatigue.2020.105646>.
9. Burns DE, Kudzal A, McWilliams B, Manjarres J, Hedges D, Parker PA (2019) Investigating additively manufactured 17–4 PH for structural applications. *J Mater Eng Perform* 28(8):4943–4951. <https://doi.org/10.1007/s11665-019-04206-9>
10. Concli F, Gilioli A (2019) Numerical and experimental assessment of the mechanical properties of 3D printed 18-Ni300 steel trabecular structures produced by Selective Laser Melting – a lean design approach. *Virtual Phys Prototyp.* <https://doi.org/10.1080/17452759.2019.1565596>
11. Concli F, Gilioli A, Nalli F (2019) Experimental–numerical assessment of ductile failure of Additive Manufacturing selective laser melting reticular structures made of Al A357. *Proc Inst Mech Eng Part C J Mech Eng Sci.* <https://doi.org/10.1177/0954406219832333>
12. Concli F, Gilioli A (2018) Numerical and experimental assessment of the static behavior of 3D printed reticular Al structures produced by selective laser melting: progressive damage and failure. *Procedia Structural Integrity.* <https://doi.org/10.1016/j.prostr.2018.11.094>
13. Hamlin RJ (2015) Microstructural evolution and mechanical properties of simulated heat affected zones in cast precipitation hardened stainless steels 17–4 and 13–8 + Mo. *Metall Mater Trans.* 48:246–264
14. Hamlin RJ, DuPont JN (2017) Microstructural evolution and mechanical properties of simulated heat-affected zones in cast precipitation-hardened stainless steels 17–4 and 13–8+Mo. *Mater Trans A Phys Metall Mater Sci Metall.* <https://doi.org/10.1007/s11661-016-3851-6>
15. Nalli F, Cortese L, Concli F (2021) Ductile damage assessment of Ti6Al4V, 17–4PH and AlSi10Mg for additive manufacturing. *Fract Mech Eng.* <https://doi.org/10.1016/j.engfracmech.2020.107395>
16. Bonaiti L, Concli F, Gorla C, Rosa F (2019) Bending fatigue behaviour of 17–4 PH gears produced via selective laser melting. *Procedia Struct Integr* 24:764–774. <https://doi.org/10.1016/j.prostr.2020.02.068>
17. ASTM E466-21 (2021) Standard practice for conducting force controlled constant amplitude axial fatigue tests of metallic materials. ASTM International, West Conshohocken, PA. <https://www.astm.org>
18. Maccioni L, Rampazzo E, Nalli F, Borgianni Y, Concli F (2021) Low-Cycle-Fatigue Properties of a 17-4 PH Stainless Steel Manufactured via Selective Laser Melting. In: *Key Engineering Materials*, vol 877. Trans Tech Publications Ltd, pp 55–60
19. C. Gorla, F. Rosa, F. Concli, and H. Albertini, 2012 “Bending fatigue strength of innovative gear materials for wind turbines gearboxes: Effect of surface coatings,” in *ASME International Mechanical Engineering Congress and Exposition, Proceedings (IMECE)*. doi: <https://doi.org/10.1115/IMECE2012-86513>
20. Gorla C, Conrado E, Rosa F, Concli F (2018) Contact and bending fatigue behaviour of austempered ductile iron gears. *Inst Mech Eng Part C J Mech Eng Sci Proc.* <https://doi.org/10.1177/0954406217695846>
21. Concli F (2018) Austempered Ductile Iron (ADI) for gears: contact and bending fatigue behavior. *Procedia Struct Integr* 8:14–23. <https://doi.org/10.1016/j.prostr.2017.12.003>
22. Gorla C, Rosa F, Conrado E, Concli F (2017) Bending fatigue strength of case carburized and nitrided gear steels for aeronautical applications. *Int J Appl Eng Res* 12(21):11306–11322
23. Dixon WJ (1965) The up-and-down method for small samples. *J Am Stat Assoc* 60(312):967–978. <https://doi.org/10.1080/01621459.1965.10480843>
24. Yadollahi A, Shamsaei N (2017) Additive manufacturing of fatigue resistant materials: challenges and opportunities. *Int J Fatigue* 98:14–31
25. Maccioni L, Fraccaroli L, Concli F (2021) High-cycle-fatigue characterization of an additive manufacturing 17-4 PH stainless steel. In: *Key Engineering Materials*, vol 877. Trans Tech Publications Ltd, pp 49–54
26. ASTM E606 / E606M-21 (2021) Standard test method for strain-controlled fatigue testing. ASTM International, West Conshohocken, PA. <https://www.astm.org>
27. ISO12111:2011 Fatigue testing – Strain controlled thermomechanical fatigue testing method
28. ASTM E739-10 (2015) Standard practice for statistical analysis of linear or linearized stress-life (S-N) and strain-life (e-N) fatigue data. ASTM International, West Conshohocken, PA. <https://www.astm.org>
29. Ramberg W, Osgood WR (1943) Description of stress-strain curves by three parameters
30. Hollomon JR (1945) Tensile deformation. *Trans AIME* 162:268–277
31. “Type 630, 17 Cr-4Ni UNS S17400.”
32. du Plessis A, Macdonald E (2020) Hot isostatic pressing in metal additive manufacturing: X-ray tomography reveals details of pore closure. *Manuf Addit.* <https://doi.org/10.1016/j.addma.2020.101191>

Publisher's Note Springer Nature remains neutral with regard to jurisdictional claims in published maps and institutional affiliations.